49th AIAA Aerospace Sciences Meeting including the New Horizons Forum and Aerospace Exposition
4 - 7 January 2011, Orlando, Florida

AIAA 2011-480

Numerical Investigation of Shock-wave/Isotropic Turbulence Interaction

Nathan E. Grube,* Ellen M. Taylor, and M. Pino Martín†
University of Maryland, College Park, MD 20742, USA

We conduct direct numerical simulations (DNS) of shock/isotropic-turbulence interactions (SITI), in which the turbulence is highly compressible. We find, consistent with previous studies using less-compressible turbulence, that turbulent kinetic energy and transverse vorticity fluctuations become persistently amplified upon passage through a shock wave and that the Taylor microscales and Kolmogorov lengthcale all diminish. Jumps in thermodynamic quantities fall short of their laminar magnitudes. In general, all of these effects tend to intensify with decreasing strength of upstream turbulence and with increasing strength of the normal shock. Comparison of individual terms for the vorticity variance budget shows that the amplification of vorticity is dominated by the compression term. Reynolds stress budgets show that downstream of the interaction, the pressure term acts to decrease the streamwise Reynolds stress and increase the transverse. Two-dimensional energy spectra show that the interaction leaves the spectrum with more energy in scales smaller than the original energetic scales. For the conditions chosen, the interaction corresponds to sharply-defined shocks across the entire wrinkled shock surface rather than distorted or broken shock fronts with regions of smooth compression. The shock structure follows the similarity scaling based on turbulent and convective Mach numbers as proposed by Donzis. (Donzis, Diego A., "Similarity Scaling in Shock-Turbulence Interactions," Presented at the 63rd Annual Meeting of the American Physical Society Division of Fluid Dynamics, Long Beach, CA, November 21-23, 2010.)

I. Introduction

The interaction of turbulence with shock waves occurs in many external and internal fluid flows, including but not limited to flows over the surfaces of fast-moving vehicles and flows within the engines of such vehicles. Strong coupling between the two phenomena and strong nonlinearities in the interaction dynamics can lead to substantial changes in the structures of both the shock wave, which may impinge on surfaces at altered locations and with altered intensities, and the passing turbulence, which may cause physical mechanisms such as energy transfer to behave differently throughout the entire downstream region. The simplest shock/turbulence interaction configuration is that of homogeneous isotropic turbulence interacting with a steadily moving normal shock wave, but because of difficulties in forming such a configuration experimentally and adequately resolving it numerically, a much larger body of work exists for interactions of shock waves with turbulent boundary layers than for interactions with isotropic turbulence. While studies of shock/turbulent-boundary-layer interactions are of great importance from the standpoints of both physics and engineering, concurrent studies of shock/isotropic-turbulence interactions (SITI) can help to elucidate which physical processes are common to shock/turbulence interaction in general and which may be unique to interactions that include boundary layers.

Agui et al.[1] have produced the only experimental work on SITI involving turbulence that closely approaches isotropy, and numerical studies of low-Reynolds-number SITI in the form of direct numerical simulations (DNS) have been conducted by Hannappel and Friedrich,[2] Lee et al.,[3] Mahesh et al.,[4] and Jamme et al.[5] Together, these investigations confirm and elaborate on, among other findings, behaviors widely believed to be true of shock/turbulence interactions in general: certain turbulence properties, notably turbulent kinetic energy and vorticity fluctuations, are amplified upon passage through a shock wave and most

*Visiting Graduate Student, University of Maryland, AIAA Member.
†Associate Professor, University of Maryland, AIAA Senior Member.

turbulent length scales, such as the Taylor microscale, are diminished. In all of these studies, however, the upstream turbulence is incompressible or at most weakly compressible. A more recent study by Larsson and Lele[6] corrects apparent resolution deficiencies in previous studies due to a persistent change in the Kolmogorov lengthscale and introduced more significant compressibility effects in the incoming turbulence. Larsson and Lele report that the stronger compressibility can lead to qualitatively different interactions where instantaneous profiles are smooth in places. Donzis[7] investigates the similarity scaling of the SITI problem and proposes nondimensional parameters in which shock structure and amplification factors show universal behavior.

In highly compressible isotropic turbulence, DNS by Passot and Pouquet,[8] Lee et al.,[9] and Samtaney et al.[10] have demonstrated the existence of small, transient shock waves known as shocklets, which due to locally strong compression are capable of affecting global flow dynamics out of proportion to their small volume fraction. It is therefore reasonable to suspect that the interaction of shock waves with highly compressible turbulence may exhibit characteristics that cannot be inferred from the results of interactions with weakly compressible turbulence. Larsson and Lele reach into the broken shock regime using combinations of convective and turbulent Mach numbers such that shocklets in the incoming turbulence do not require shock-capturing.

The purpose of this paper is to describe direct numerical simulations of highly-compressible isotropic turbulence with strong shocklets interacting with a normal shock wave, and to ascertain physically relevant flow characteristics and processes from the resulting data. Sections II and III present governing equations and the numerical methods employed to compute them. In Sections IV, V and VI, we describe the computational configuration, auxiliary forced isotropic simulation, and flow conditions of the conducted SITI simulations. Section VII introduces our approaches to data analysis, Section VIII presents the results, and conclusions are drawn in Section IX.

II. Governing Equations

Shock/isotropic-turbulence interaction is governed by the three-dimensional compressible Navier-Stokes equations describing conservation of mass, momentum, and energy,

$$\frac{\partial \rho}{\partial t} + \frac{\partial}{\partial x_j}\left(\rho u_j\right) = 0 \tag{1}$$

$$\frac{\partial}{\partial t}\left(\rho u_i\right) + \frac{\partial}{\partial x_j}\left(\rho u_i u_j + p\,\delta_{ij} - \sigma_{ij}\right) = 0 \tag{2}$$

$$\frac{\partial}{\partial t}\left(\rho e\right) + \frac{\partial}{\partial x_j}\left[\left(\rho e + p\right) u_j - \sigma_{ij} u_i + q_j\right] = 0 \tag{3}$$

in which ρ is density, u_i is velocity in the i direction, p is pressure, and e is total energy per unit mass. The viscous stress tensor σ_{ij} is assumed to obey a linear stress-strain relationship,

$$\sigma_{ij} = \mu\left[\left(\frac{\partial u_i}{\partial x_j} + \frac{\partial u_j}{\partial x_i}\right) - \frac{2}{3}\frac{\partial u_k}{\partial x_k}\delta_{ij}\right] \tag{4}$$

in which viscosity μ depends only on temperature T through a power law[11] of the form

$$\mu = \mu_0\left(\frac{T}{T_0}\right)^n \tag{5}$$

in which μ_0 and T_0 are reference values that depend on the particular gas mixture. The heat flux q_i is computed through Fourier's law of heat conduction,

$$q_i = -k\frac{\partial T}{\partial x_i} \tag{6}$$

in which k is thermal conductivity.

The working fluid is air, which is treated as a perfect gas with gas constant $R = 287.1\,\mathrm{m}^2/\mathrm{s}^2K$ and constant specific heat capacity (at constant volume) $c_v = \frac{5}{2}R$. Therefore $P = \rho RT$, in which T is temperature; the speed of sound $a = \sqrt{\gamma RT}$, in which the heat capacity ratio $\gamma = \frac{7}{5}$; and

$$e = c_v T + \tfrac{1}{2} u_k u_k \tag{7}$$

The reference viscosity μ_0 is taken to be $1.789 \times 10^{-5}\,\mathrm{kg/m\,s}$ at a reference temperature $T_0 = 288.2\,\mathrm{K}$ in accordance with the standard atmosphere at sea level, and the exponent n in Eq. (5) is taken to be 0.76. The thermal conductivity k is assumed to be proportional to the viscosity μ with a constant of proportionality equal to $\left(c_v + \frac{9}{4}R\right)$.[12]

III. Numerical Methods

The detailed simulation of compressible turbulence requires numerical methods that simultaneously avoid excessive damping of spatial features over a large range of length scales and prevent spurious oscillations near shocks and shocklets through robust shock-capturing. Numerical schemes that were developed to satisfy these constraints include, among others, weighted essentially non-oscillatory (WENO) methods.[13,14] WENO schemes compute numerical fluxes using several different candidate stencils and form a final flux approximation by summing weighted contributions from each stencil. Thus they are nonlinear. Smoothness measurements cause stencils that span large flow field gradients to be assigned small relative weights so that a nearly discontinuous shock would provide a weight of almost zero to any stencil containing it. In smooth regions, the relative values of the weights are designed to be optimal by some gauge such as maximum order of accuracy or maximum bandwidth-resolving efficiency. Martín et al.[15] demonstrate that a bandwidth-optimized symmetric WENO method[15–17] provides accurate results for direct numerical simulations of compressible isotropic turbulence and turbulent boundary layers. Therefore, in the current work, we employ a fourth-order-accurate version of this scheme to compute the convective terms of the governing equations.

To compute the viscous terms, we employ a simple fourth-order-accurate standard central difference scheme; and to integrate over time, we employ the third-order-accurate, low-storage Runge-Kutta method of Williamson[18] with a CFL number of 0.5.

IV. Computational Configuration

The inflow for the SITI simulations is supersonic and is prescribed using data from an auxiliary isotropic turbulence simulation. The flow parameters under consideration here preclude the use of Taylor's Hypothesis to convect "frozen" turbulence through the inflow plane. Taylor's Hypothesis relies on the velocity fluctuations being much smaller than the mean velocity, which is not true for sufficiently vigorous incoming turbulence as in the cases considered here. Therefore, the inflow turbulence is prescribed using temporally-saved data from a forced isotropic turbulence simulation. The physical domain for the inflow simulation is a three-dimensional elongated box with periodic boundary conditions. The box has edges of length $L = 4 * 2\pi/\kappa_0$ where κ_0 is the most energetic wavenumber in the initial spectrum. The edge length is therefore four times the most energetic wavelength; an evenly-spaced Cartesian grid discretizes this domain with equal spacing in all directions.

Three non-dimensional parameters characterize the state of the incoming turbulent flow: the Reynolds number based on the Taylor microscale

$$Re_\lambda = \frac{\langle\rho\rangle\, u'_{\mathrm{rms}}\, \lambda}{\langle\mu\rangle} \tag{8}$$

in which u'_{rms} is the root-mean-squared fluctuating velocity (per component) and λ is the Taylor microscale; the turbulent Mach number

$$M_t = \frac{q}{\langle a\rangle} \tag{9}$$

in which a is the speed of sound and q is the root-mean-squared fluctuating velocity magnitude; and the convective Mach number

$$M = \frac{\langle\rho u\rangle}{\langle\rho\rangle\,\langle a\rangle}. \tag{10}$$

For the SITI simulation, the domain size in directions perpendicular to the mean flow is determined by the edge length L of the forced isotropic turbulence field. Useful domain size parallel to the mean flow, which

is chosen to be aligned with the x-axis, is designated L_x. In the current work, $L_x = \frac{1}{2}L$. Within L_x there are N_x grid points in the streamwise direction, which are chosen to match the resolution in the transverse directions. The domain is periodic in the two transverse directions.

After interacting with the main shock wave, the altered turbulence field approaches the outflow boundary at subsonic speed. We use an L_s-wide sponge zone[4,19] in concert with a characteristic-based approximately non-reflecting boundary condition[20] at the exit plane to avoid acoustic reflections. In the present work, $L_s = \frac{1}{2}L_x$. The sponge region damps fluctuations and moves the flow toward a target constant state (the initial laminar post-shock state). The single inward-traveling characteristic at the outflow gives one degree of freedom which could be used to specify the pressure at the outflow boundary. Rather than specify a fixed pressure, we choose to compute only outward-traveling waves, thus allowing the pressure to float at the outflow plane. However, the pressure is still driven toward a desired outflow value by the sponge zone leading up to the outflow. This target outflow pressure is chosen to be slightly different from the post-shock state for a given nominal Mach number in order to control shock drift due to the turbulence. The proper choice of exit pressure is not known ahead of time due to the inapplicability of the Rankine-Hugoniot jump conditions to mean quantities as opposed to instantaneous quantities. Multiple simulations are used to determine the correct exit pressure as the solution to a root-finding problem. The exit pressure is refined until the drift over the period of gathering statistics is at least an order of magnitude smaller than the extent of the interaction region.

A sketch of the entire computational domain resulting from all of these arrangements is provided by Fig. 1. While statistical quantities in isotropic turbulence are aggregated over three spatial dimensions at each point in time, in SITI they are aggregated over time and the two spanwise dimensions at each streamwise location. We define $\langle\eta\rangle$ as the time- and spanwise-aggregated average of a generic quantity η, η' as the associated root-mean-squared deviation (*not* the local deviation), and $\langle\langle\eta\rangle\rangle$ and η'' as the corresponding density-weighted (Favre) average and root-mean-squared deviation, respectively.

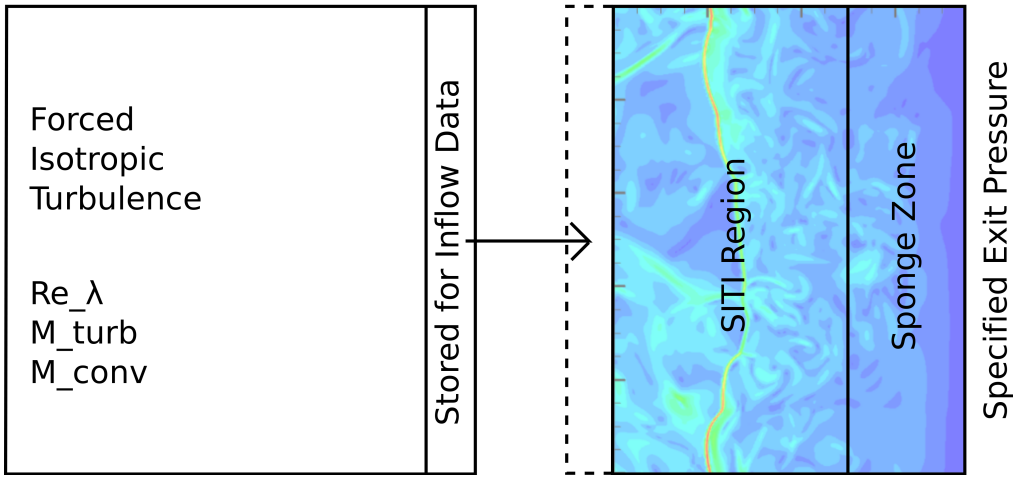

Figure 1. Computational domain sketch for shock/isotropic-turbulence interaction.

V. Isotropic Inflow Turbulence

A randomized solenoidal approximation[21] to isotropic turbulence with most-energetic wavenumber $\kappa_0 = 4$ serves as an initial turbulent flowfield for the auxiliary forced computation, and to transform it into realistic turbulence, we evolve this field through a transient period lasting $1.5\tau_t$, where τ_t is the initial state's reference time λ/u'_{rms}. Additional details about our isotropic simulations can be found in Taylor and Martín.[22] After this period of decaying evolution, the spectrum is computed and used as a target spectrum for a forced isotropic simulation.

The forcing scheme of Overholt and Pope[23] for isotropic turbulence is used to maintain a stationary state of inflow turbulence. The forcing acts in wavenumber space and amplifies the lowest wavenumber modes without changing their phases. The forcing scheme adds energy as needed to prevent the computed energy spectrum from falling significantly below a model or target spectrum, $E_m(\kappa)$. Each mode evolves in time

according to the differential equation

$$\frac{\partial \hat{\mathbf{u}}(\boldsymbol{\kappa}, t)}{\partial t} = \hat{\mathbf{a}}(\boldsymbol{\kappa}, t) + \frac{f_\kappa(t)}{\tau_f}\hat{\mathbf{u}}(\boldsymbol{\kappa}, t)$$

where $\hat{\mathbf{a}}(\boldsymbol{\kappa}, t)$ is the Fourier transform of the usual Navier-Stokes equation terms, $f_\kappa(t)$ is the forcing coefficient for the Fourier modes in the κ-shell, and τ_f is the forcing timescale. The coefficients $f_\kappa(t)$ evolve according to

$$\frac{\mathrm{d}f_\kappa(t)}{\mathrm{d}t} = P\left[\frac{-1}{\tau_f}\ln\left(\frac{E(\kappa,t)}{E_m(\kappa)Z_f(\kappa)}\right) - \alpha\alpha_c f_k(t)\right] = P\left[S_\kappa\right]$$

where α is a dimensionless damping parameter (taken here to be 1), $\alpha_c = 2\sqrt{2}/\tau_f$ is the damping coefficient giving critical damping, and P is an operator defined by

$$P\left[S_\kappa\right] = \begin{cases} S_\kappa \text{ for } f_\kappa \geq 0 \\ S_\kappa \text{ for } f_\kappa = 0 \text{ and } S_\kappa > 0 \\ 0 \text{ for } f_\kappa = 0 \text{ and } S_\kappa \leq 0 \end{cases}$$

The forcing cut-off function $Z_f(\kappa)$ is defined by

$$Z_f(\kappa; \kappa_f, \zeta) = \tanh\left(\frac{\kappa_f - \kappa}{\zeta\kappa_f}\right) H(\kappa_f - \kappa)$$

where κ_f is the wavenumber at which the forcing goes to zero, and, in this paper, $\zeta = 0.2$. The forcing timescale is related to the Kolmogorov timescale by the dimensionless parameter

$$T_f^* = \left(\frac{\tau_f}{\tau_\eta}\right)$$

which is here taken to be $T_f^* = 0.3$.

Overholt and Pope designed this forcing procedure for incompressible flow. To use it in a compressible flow, two modifications are made to their procedure. First, in order to prevent an unbounded increase in average temperature due to the addition of energy via forcing, the total energy added by the forcing term is subtracted from the conservation equation for total energy in a spatially-uniform manner. This holds the global total energy of the flow constant while still preserving the local changes in energy due to the forcing. The results appear to be insensitive to the details of the energy removal. Simulations run with the local rate of thermal energy removal matched to the local rate of energy addition gave nearly identical results. Second, the amplification of velocity Fourier modes combined with the nonuniform density of a compressible turbulence field leads to small changes in the global momentum. In order to prevent the development over time of significant mean velocity drift, a spatially-uniform body force is applied to exactly cancel out any global addition of momentum due to the forcing. With these two modifications, the forcing method can provide a statistically stationary turbulent field with a desired spectrum and with constant global mass, momentum, and energy. No complications arise with the specification of a constant mean convection velocity.

VI. Flow Conditions

The inflow isotropic turbulence field is initialized with nominal Reynolds number $(Re_\lambda)_0$, nominal turbulent Mach number $(M_t)_0$, nominal convective Mach number $(M)_0$ and sea-level atmospheric thermodynamic conditions and then evolved until $t = 1.5\tau_t$ when the initialization transient has sufficiently subsided. The isotropic field is then used at the initial condition for forced isotropic turbulence simulation to generate stationary inflow data. The stationary state reached by the forcing procedure is characterized by inlet parameters $(Re_\lambda)_1$, $(M_t)_1$, and $(M)_1$. The Reynolds numbers and turbulence and convective Mach numbers all decrease from their initial values due to the decay of the turbulence fluctuations and a rise in the mean temperature between initialization and the time that the forcing reaches a stationary state. Table 1 lists the physical and computational parameters for the SITI simulation that we conduct. We consider three cases, labeled C1, C2, and C3. All share initial Reynolds number $(Re_\lambda)_0 = 35$. In order to investigate the influence of M_t, we change $(M_t)_0$ from 0.7 to 1.3 in cases C1 and C2 while leaving $(M)_0 = 3.5$, which is the smallest convective speed that will safely ensure supersonic inflow at all points. To investigate the influence of M, we change $(M)_0$ from 3.5 to 5.0 in cases C2 and C3 while leaving $(M_t)_0 = 1.3$. The changes in parameters between the inlet and the interaction region is small.

Case	C1	C2	C3
M_0	3.5	3.5	5
$(Re_\lambda)_0$	35	35	35
$(M_t)_0$	0.7	1.3	1.3
M_1	3.46	3.31	4.66
$(Re_\lambda)_1$	26	22	22
$(M_t)_1$	0.52	0.86	0.85
N^2	300^2	300^2	300^2
N_x+N_s	150+75	150+75	150+75

Table 1. Physical and computational parameters for conducted simulations of shock/isotropic-turbulence interaction.

VII. Approaches to Data Analysis

Before presenting the results in the next section, we establish groundwork regarding the analysis of the three-dimensional unsteady flow data of shock/isotropic-turbulence interaction. The analysis includes plots of streamwise profiles of time- and spanwise-averaged flow properties, including vorticity fluctuations, Taylor microscale and Kolmogorov scale, and budgets of vorticity and Reynolds stresses; and plots of time-averaged two-dimensional kinetic energy spectra at key streamwise locations.

Budgets of vorticity and Reynolds stresses serve to segregate total changes in these two properties into contributions from different physical processes. Conservation of vorticity is characterized by the following adaptation of Eq. (2):

$$\frac{D\vec{\omega}}{Dt} = \left(\vec{\omega}\cdot\vec{\nabla}\right)\vec{u} - \vec{\omega}\left(\vec{\nabla}\cdot\vec{u}\right) + \frac{1}{\rho^2}\vec{\nabla}\rho\times\vec{\nabla}p + \vec{\nabla}\times\frac{1}{\rho}\left(\vec{\nabla}\cdot\vec{\bar{\sigma}}\right) \tag{11}$$

in which $\vec{\omega}$ is the vorticity vector and $\frac{D}{Dt}$ is the material derivative operator. From left to right, the quantities on the right-hand side of this equation describe stretching and tilting due to velocity gradients, stretching due to flow compressibility, changes due to the misalignment of density and pressure surfaces, and changes due to diffusion. We refer to them as the stretching, compressible, baroclinic, and diffusion terms, respectively. All terms in (11) average to zero in SITI, so we take the product of the α-component of (11) with ω_α to find the contributions of each term to the budget for the variance of α-vorticity $\langle\omega_\alpha\omega_\alpha\rangle$.

Conservation of Reynolds stresses is characterized by the following alternative adaptation of Eq. (2), which omits certain negligible terms that approach zero as the flow approaches incompressibility:

$$\frac{\langle\langle D\rangle\rangle}{\langle\langle D\rangle\rangle t}R_{ij} = -\frac{\partial}{\partial x_k}T_{ijk} + \mathscr{P}_{ij} + \Pi_{ij} + \phi_{ij} - \varepsilon_{ij} \tag{12}$$

in which

$$\frac{\langle\langle D\rangle\rangle}{\langle\langle D\rangle\rangle t} = \frac{\partial}{\partial t} + \langle\langle u_k\rangle\rangle\frac{\partial}{\partial x_k} \tag{13}$$

$$R_{ij} = \langle\rho\rangle\left[\langle\langle u_i u_j\rangle\rangle - \langle\langle u_i\rangle\rangle\langle\langle u_j\rangle\rangle\right] \tag{14}$$

$$T_{ijk} = \left\langle\rho u_i'' u_j'' u_k''\right\rangle \tag{15}$$

$$\mathscr{P}_{ij} = -R_{jk}\frac{\partial\langle\langle u_i\rangle\rangle}{\partial x_k} - R_{ik}\frac{\partial\langle\langle u_j\rangle\rangle}{\partial x_k} - R_{ij}\frac{\partial\langle\langle u_k\rangle\rangle}{\partial x_k} \tag{16}$$

$$\Pi_{ij} = -\left\langle u_i''\frac{\partial p'}{\partial x_j} + u_j''\frac{\partial p'}{\partial x_i}\right\rangle \tag{17}$$

$$\phi_{ij} = \frac{\partial}{\partial x_k}\left\langle u_i''\sigma_{jk}' + u_j''\sigma_{ik}'\right\rangle \tag{18}$$

$$\varepsilon_{ij} = \left\langle\sigma_{jk}'\frac{\partial u_i''}{\partial x_k} + \sigma_{ik}'\frac{\partial u_j''}{\partial x_k}\right\rangle \tag{19}$$

and, in this instance only, the prime and double-prime superscripts indicate instantaneous rather than root-mean-squared deviations. From left to right, the quantities on the right-hand side of Eq. (12) are known as the turbulent convection, production, pressure, viscous diffusion, and viscous dissipation terms.

As stated previously, streamwise profiles of flow properties are created by statistically aggregating local instantaneous values over time and the two spanwise spatial dimensions at each streamwise location. Although we adjust the exit pressure to mitigate the shock drift, the passing turbulent fluctuations still lead to substantial random streamwise motion and corrugation of the main shock wave. Therefore, the shock's broad effects on that turbulence cannot be localized to a single streamwise location but are rather spread over a range. Let us define $\langle x_s \rangle_{\min}$ as the minimum instantaneous spanwise-averaged position, $\langle x_s \rangle_{\max}$ as the maximum instantaneous average, and x_s' as the time-averaged root-mean-squared deviation from instantaneous average. In all plots of streamwise profiles, a shaded region bounded by dashed lines will denote the region between $\langle x_s \rangle_{\min}$ and $\langle x_s \rangle_{\max}$, and dotted lines upstream and downstream of this region will denote, respectively, $\langle x_s \rangle_{\min} - x_s'$ and $\langle x_s \rangle_{\max} + x_s'$. We consider the entire area between the latter bounds to constitute the interaction region.

Determining the instantaneous local streamwise positions of the main shock wave, which are necessary for computing the statistical quantities above, is in general not trivial to accomplish both accurately and efficiently. We begin by identifying, for each point in time separately, the m strongest density and pressure gradients along a streamwise line through each spanwise grid location under the assumption that such gradients must traverse either the main shock wave or especially strong shocklets. These locations are then ranked by how closely the strengths of the shock wave sections that coincide with them conform to the prescribed average strength of the main shock wave. We use the single most attractive candidate position (according to this ranking) at each spanwise location to calculate a preliminary instantaneous average streamwise position and root-mean-squared deviation; we then temporarily discard any points that lie more than twice this root-mean-squared deviation away from this average; and we use the remaining points to calculate a new conditionally spanwise-averaged main shock position. For the outlier points that were temporarily discarded, we substitute whichever one of the m candidates at those spanwise locations that minimizes deviation from the conditional average under the assumption that the main shock wave should be relatively continuous. In all conducted SITI simulations, we find that setting $m = 2$ provides sufficient accuracy.

Finally, at key streamwise locations, we compute the two-dimensional turbulent kinetic energy spectrum

$$E(k) = \int_{|\vec{\kappa}|=k,\ \kappa_1=0} \tfrac{1}{2} \left[\hat{u}_2(\vec{\kappa}) \cdot \hat{u}_2(\vec{\kappa}) + \hat{u}_3(\vec{\kappa}) \cdot \hat{u}_3(\vec{\kappa}) \right] \mathrm{d}\vec{\kappa} \tag{20}$$

in which carats indicate Fourier transforms and k is wavenumber magnitude.

VIII. Results

A. General SITI results

We first confine our attention to case C1 to investigate features of SITI common to all cases.

The interaction has a great impact on the vorticity of the turbulent field (Fig. 2). The root-mean-square transverse vorticity fluctuation is amplified by the interaction, but there is little immediate change in the streamwise component. After a lag, the streamwise component begins to grow and the transverse component decays until the fluctuating vorticity approaches isotropy near the end of the useful domain.

The vorticity amplification can be better understood by analyzing the vorticity conservation budget (11) term-by-term. The contributions of the individual terms in the vorticity budget are plotted in Fig. 3. The strong amplification of transverse fluctuations is primarily due to the compressible term, with negligible contribution by the baroclinic and stretching terms. The compressible and stretching terms approximately cancel in the streamwise case at the beginning of the interaction region. In the downstream turbulence, there is an approximate balance between a viscous diffusion sink and stretching source.

The interaction also amplifies turbulent kinetic energy (TKE) and Reynolds stresses (Fig. 4). The shock motion produces a peak which is followed by persistently elevated levels of TKE and Reynolds stresses. The post-interaction turbulence is anisotropic, with the streamwise stresses greater than the transverse.

The contributions of the terms in the Reynolds stress budget (12) are plotted in Fig. 5. Upstream of the interaction, the Reynolds stress budgets are dominated by the viscous dissipation term. Across the

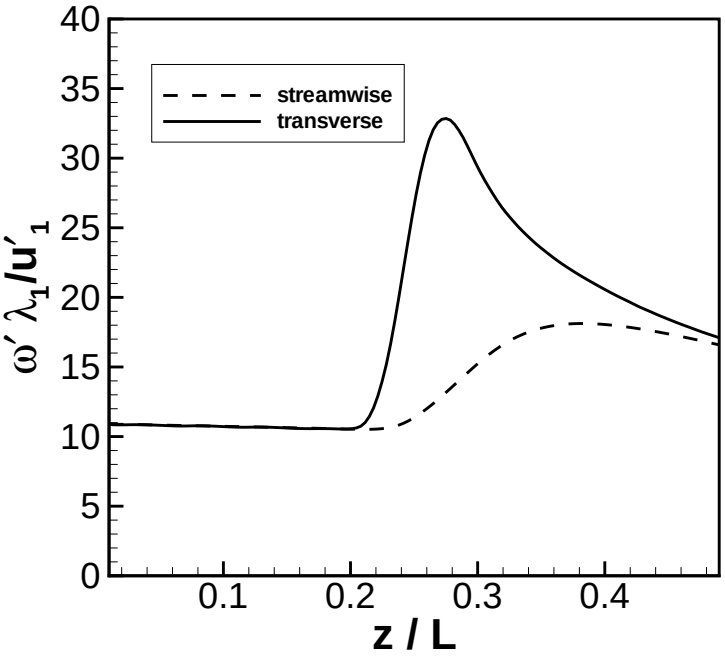

Figure 2. Profiles of rms vorticity fluctuations in streamwise and transverse directions for case C1 ($M_1 = 3.46$, $M_t = 0.52$, $Re_\lambda = 26$).

interaction region, then terms fluctuate wildly, and downstream of the interaction, the turbulence is in a state of disequilibrium, again with a strong contribution by vsicous dissipation, but now also with a contribution by the pressure term which tends to redistribute TKE from the streamwise to transverse Reynolds stress components.

The interaction also modifies the energy spectrum of the passing turbulence (Fig. 6). Upstream of the interaction, the spectrum changes only slowly with streamwise distance. We therefore plot the spectrum at only one upstream station. Across the interaction region, the spectrum changes shape, with slightly less energy in the energetic modes but with a much fuller tail. This may be due in part to the corrugated shock passing through the plane and contributing near-discontinuities to the velocity field. Downstream of the interaction, the spectrum returns to a new, almost constant, shape with increased energy content in scales smaller than the original energetic scales. This suggests that the transverse Reynolds stress growth is due to increased energy at these smaller scales.

B. Effect of M_t

The Rankine-Hugoniot jump conditions apply instantaneously, but not in the mean. The presence of turbulent fluctuations acts to decrease the magnitudes of thermodynamic jumps across a shock. Figure 7 plots the density jumps across the nominally Mach 3.5 normal shock for cases C1 ($M_t = 0.52$) and C2 ($M_t = 0.86$). The equivalent laminar jumps are plotted for comparison. The stronger turbulence clearly leads to a much greater deviation from the Rankine-Hugoniot jump condition.

Contours of instantaneous density gradient magnitudes in Fig. 8 show qualitatively how the SITI flow changes with M_t. The higher M_t of case C2 leads to a more wrinkled or corrugated shock front as well as a less obvious change in the turbulence scales and intensity.

The Taylor microscales and the Kolmogorov lengthscale are all diminished by the interaction and maintain values downstream of the shock than upstream (Fig. 9). This effect is lessened by stronger upstream turbulence.

The amplifications of turbulent kinetic energy (TKE) and Reynolds stresses are diminished by stronger upstream turbulence (Fig. 10). The level of isotropy does not change significantly with M_t.

C. Effect of M

Figure 11 plots the density jumps across the normal shock for cases C2 ($M = 3.31$) and C3 ($M = 4.66$). The equivalent laminar jumps are plotted for comparison. The stronger shock of case C3 leads to a greater density jump, and the density jump deficiency increases in absolute terms, but the fractional deficiency in the density jump actually decreases slightly.

Contours of instantaneous density gradient magnitudes in Fig. 12 show qualitatively how the SITI flow changes with M. The higher M of case C3 leads to a straighter shock front as well as a greater change in the turbulence scales and intensity.

The alteration of the Taylor microscales and the Kolmogorov lengthscale by the interaction are all only weakly dependent on M (Fig. 13).

The amplifications of turbulent kinetic energy (TKE) and Reynolds stresses are increased by a stronger normal shock. The level of isotropy does not change significantly with M.

D. Similarity Scaling

Following Larsson and Lele,[6] Donzis[7] defines a quantity $\Theta = \left\langle (\theta - \langle\theta\rangle)^2 \right\rangle^{1/2} / \langle\theta\rangle$ where $\theta = |\nabla \cdot \vec{u}|_{\text{shock}}$. The quantity is the ratio of rms to mean value of the dilatation at the shock and can be used as a measure of the shock structure. A low value indicates a uniform shock front, and a large value indicates a wrinkled or even broken shock front with the possibility of areas of smooth compression. Donzis[7] has proposed that the shock structure as measured by the normalized root-mean-square shock dilation Θ is universal in the parameter $M_t/(M-1)$, and that amplification factors such as $G_{u''^2} \equiv u''^2_{\text{d}}/u''^2_{\text{u}}$, where subscripts u and d denote upstream and downstream values, are universal in the parameter $K \equiv M_t/Re_\lambda^{1/2}(M-1)$. Figure 15 compares the current results for normalized rms shock dilatation to numerical data compiled by Donzis. Also shown is an approximate best-fit line $\theta = 0.5(M_t/(M-1)) + 0.115(M_t/(M-1))^3$. Figure 16 compares the current results for the streamwise velocity fluctuation variance amplification factor $G_{u''^2}$ to numerical and experimental data compiled by Donzis. Also shown is an empirical fit curve from Donzis. The current results support the conclusions of Donzis regarding the shock structure, but the current amplification factors for cases C1 ($K = 0.0415$, $G_{u''^2} = 2.09$) and C3 ($K = 0.0495$, $G_{u''^2} = 2.35$) are greater than predicted. The amplification factor for case C2 ($K = 0.0794$, $G_{u''^2} = 1.57$) is close to the prediction. The amplification factors from Agui et al.[1] (as great as $G_{u''^2} \approx 4$, not shown) are also significantly greater than predicted by the proposed scaling. Taken together, these results may indicate that the amplification factor scaling is not fully described by the parameter K.

IX. Conclusion

We have presented a direct numerical simulation of highly-compressible isotropic turbulence, with turbulence Mach numbers M_t ranging from 0.5 to 0.9 convecting through a nominally normal shock wave at convective Mach numbers ranging from 3.3 to 4.7. We find, consistent with previous studies using less-compressible turbulence, that turbulent kinetic energy and transverse vorticity fluctuations become persistently amplified upon passage through a shock wave and that the Taylor microscales and Kolmogorov lengthcale all diminish. Jumps in thermodynamic quantities fall short of their laminar magnitudes. In general, all of these effects tend to intensify with decreasing strength of upstream turbulence and with increasing strength of the normal shock. Comparison of individual terms for the vorticity variance budget shows that the amplification of vorticity is dominated by the compression term. Reynolds stress budgets show that downstream of the interaction, the pressure term acts to decrease the streamwise Reynolds stress and increase the transverse. Two-dimensional energy spectra show that the interaction leaves the spectrum with more energy in scales smaller than the original energetic scales. For the conditions chosen, the interaction corresponds to sharply-defined shocks across the entire wrinkled shock surface rather than distorted or broken shock fronts with regions of smooth compression. The shock structure follows the similarity scaling proposed by Donzis,[7] but the current streamwise velocity variance amplification factors for cases C1 and C3 are greater than predicted by the proposed scaling.

Acknowledgments

This work is sponsored in part by NASA Constellation University Project (CUIP) Grant #NCC3-989 and AFRL.

References

[1]Agui, J. H., Briassulis, G., and Andreopoulos, Y., "Studies of interactions of a propagating shock wave with decaying grid turbulence: velocity and vorticity fields," *Journal of Fluid Mechanics*, Vol. 524, 2005, pp. 143–95.

[2]Hannappel, R. and Friedrich, R., "Direct numerical simulation of a Mach 2 shock interacting with isotropic turbulence," *Applied Scientific Research*, Vol. 54, No. 3, 1995, pp. 205–21.

[3]Lee, S., Lele, S. K., and Moin, P., "Interaction of isotropic turbulence with shock waves: Effect of shock strength," *Journal of Fluid Mechanics*, Vol. 340, 1997, pp. 225–47.

[4]Mahesh, K., Lele, S. K., and Moin, P., "The influence of entropy fluctuations on the interaction of turbulence with a shock wave," *Journal of Fluid Mechanics*, Vol. 334, 1997, pp. 353–79.

[5]Jamme, S., Cazalbou, J.-B., Torres, F., and Chassaing, P., "Direct numerical simulation of the interaction between a shock wave and various types of isotropic turbulence," *Flow, Turbulence and Combustion*, Vol. 68, No. 3, 2002, pp. 227–68.

[6]Larsson, J. and Lele, S. K., "Direct Numerical Simulation of Canonical Shock/Turbulence Interaction," *Phys. Fluids*, Vol. 21, Dec. 2009, pp. 126101 (12 pages).

[7]Donzis, D., "Similarity Scaling in Shock-Turbulence Interactions," Presented at the 63rd Annual Meeting of the American Physical Society Division of Fluid Dynamics, Long Beach, CA, November 21-23, 2010.

[8]Passot, T. and Pouquet, A., "Numerical simulation of compressible homogeneous flows in the turbulent regime," *Journal of Fluid Mechanics*, Vol. 181, 1987, pp. 441–66.

[9]Lee, S., Lele, S. K., and Moin, P., "Eddy shocklets in decaying compressible turbulence," *Physics of Fluids A*, Vol. 3, No. 4, 1991, pp. 657–64.

[10]Samtaney, R., Pullin, D. I., and Kosović, B., "Direct numerical simulation of decaying compressible turbulence and shocklet statistics," *Physics of Fluids*, Vol. 13, No. 5, 2001, pp. 1415–30.

[11]White, F. M., *Viscous Fluid Flow*, McGraw-Hill, 2nd ed., 1991.

[12]Vincenti, W. G. and Kruger, C. H., *Introduction to Physical Gas Dynamics*, John Wiley and Sons, 1965.

[13]Liu, X.-D., Osher, S., and Chan, T., "Weighted Essentially Non-Oscillatory Schemes," *Journal of Computational Physics*, Vol. 115, No. 1, 1994, pp. 200–12.

[14]Jiang, G.-S. and Shu, C.-W., "Efficient implementation of weighted ENO schemes," *Journal of Computational Physics*, Vol. 126, No. 1, 1996, pp. 202–28.

[15]Martín, M. P., Taylor, E. M., Wu, M., and Weirs, V. G., "A bandwidth-optimized WENO scheme for the effective direct numerical simulation of compressible turbulence," *Journal of Computational Physics*, Vol. 220, No. 1, 2006, pp. 270–89.

[16]Weirs, V. G. and Candler, G. V., "Optimization of weighted ENO schemes for DNS of compressible turbulence," Paper 1997–1940, American Institute of Aeronautics and Astronautics, 1997.

[17]Weirs, V. G., *A Numerical Method for the Direct Simulation of Compressible Turbulence*, Ph.D. thesis, University of Minnesota, December 1998.

[18]Williamson, J. H., "Low-storage Runge-Kutta schemes," *Journal of Computational Physics*, Vol. 35, No. 1, 1980, pp. 48–56.

[19]Israeli, M. and Orszag, S. A., "Approximation of radiation boundary conditions," *Journal of Computational Physics*, Vol. 41, No. 1, 1981, pp. 115–35.

[20]Thompson, K. W., "Time dependent boundary conditions for hyperbolic systems," *Journal of Computational Physics*, Vol. 68, No. 1, 1987, pp. 1–24.

[21]Ristorcelli, J. R. and Blaisdell, G. A., "Consistent initial conditions for the DNS of compressible turbulence," *Phys. Fluids*, Vol. 9, 1997, pp. 4.

[22]Taylor, E. M. and Martín, M. P., "Stencil adaptation properties of a WENO scheme in direct numerical simulations of compressible turbulence," *Journal of Scientific Computing*, Vol. 30, No. 3, 2007, pp. 533–54.

[23]Overholt, M. R. and Pope, S. B., "A Deterministic Forcing Scheme for Direct Numerical Simulations of Turbulence," *Computers and Fluids*, Vol. 27, No. 1, 1998, pp. 11–28.

[24]Lee, S., Lele, S. K., and Moin, P., "Direct Numerical Simulation of Isotropic Turbulence Interacting with a Weak Shock Wave," *Journal of Fluid Mechanics*, Vol. 251, 1993, pp. 533–62.

[25]Hannappel, R. and Friedrich, R., "Direct numerical simulation of a Mach-2 shock interacting with isotropic turbulence," *Appl. Sci. Res.*, Vol. 54, 1995, pp. 205–21.

[26]Barre, S., Alem, D., and Bonnet, J. P., "Experimental Study of a Normal Shock/homogeneous Turbulence Interaction," *AIAA J.*, Vol. 34, 1996, pp. 968–74.

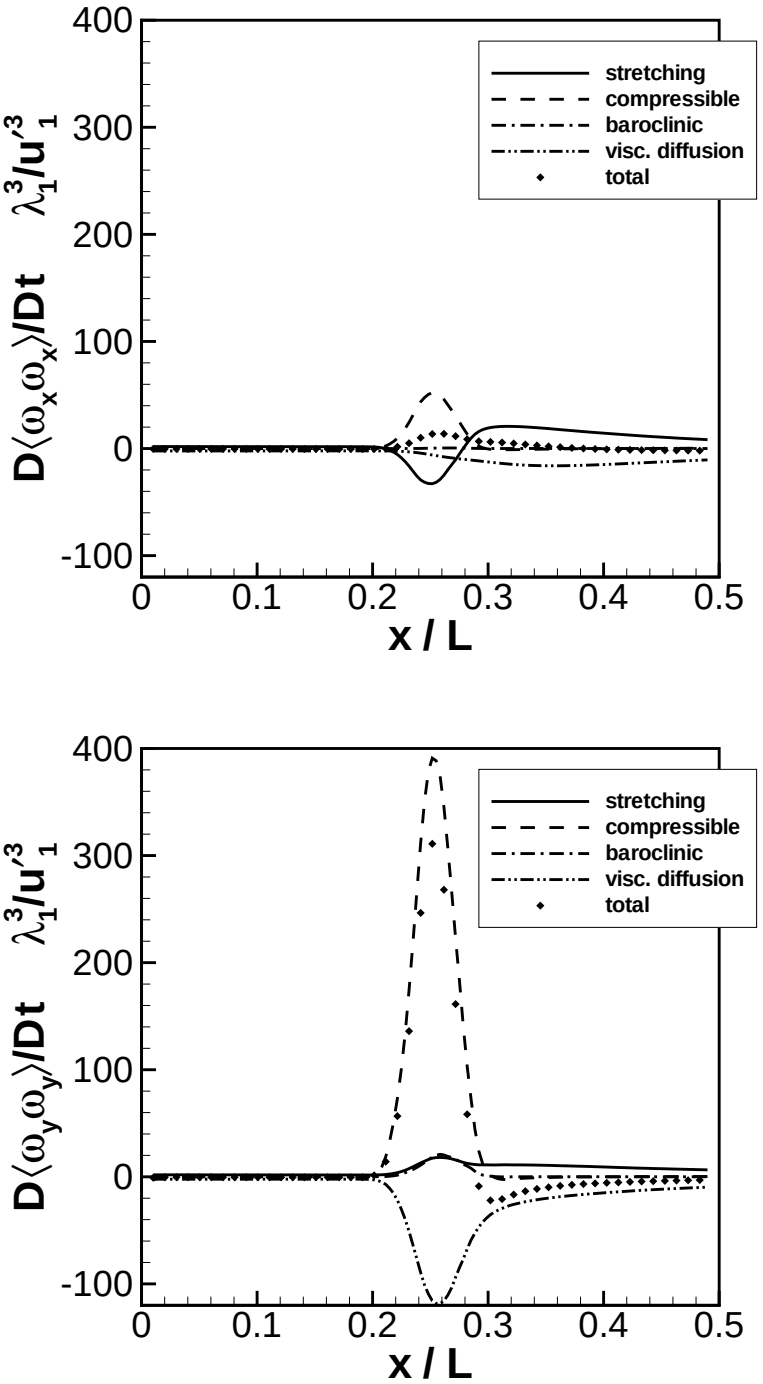

Figure 3. Contributions of individual terms in budget for *(a)* streamwise and *(b)* transverse vorticity variance for case C1 ($M_1 = 3.46$, $M_t = 0.52$, $Re_\lambda = 26$).

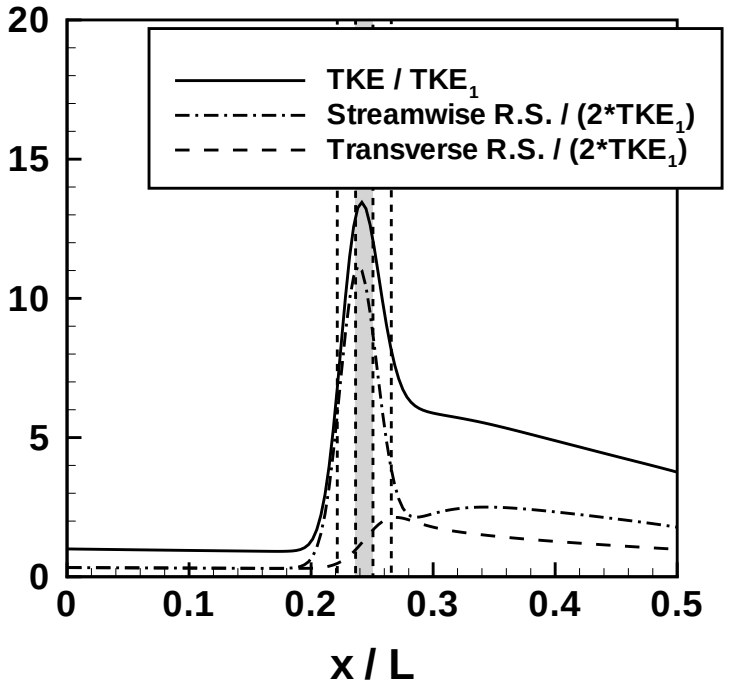

Figure 4. Profiles of turbulent kinetic energy and Reynolds stresses in streamwise and transverse directions for case C1 ($M_1 = 3.46$, $M_t = 0.52$, $Re_\lambda = 26$).

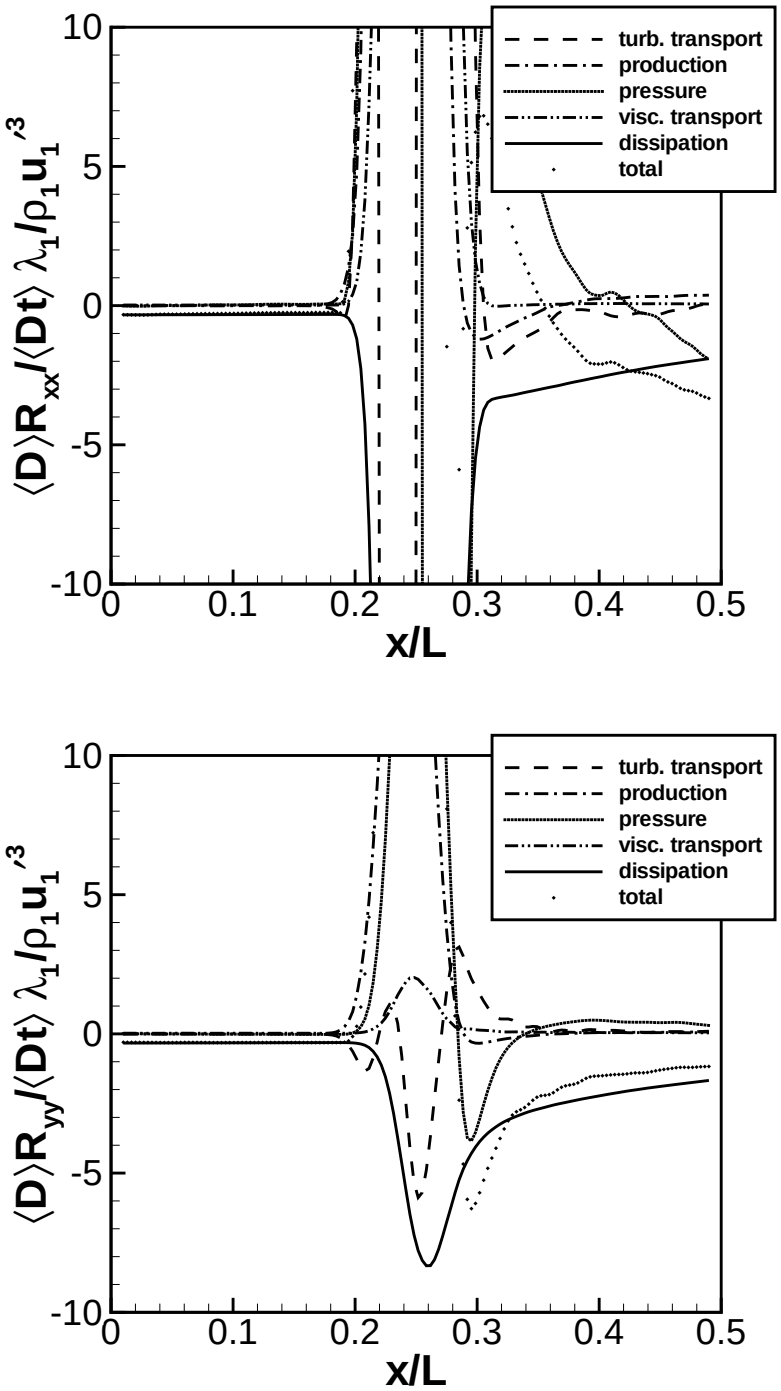

Figure 5. Contributions of individual terms in budget for *(a)* streamwise and *(b)* transverse Reynolds stress for case C1 ($M_1 = 3.46$, $M_t = 0.52$, $Re_\lambda = 26$).

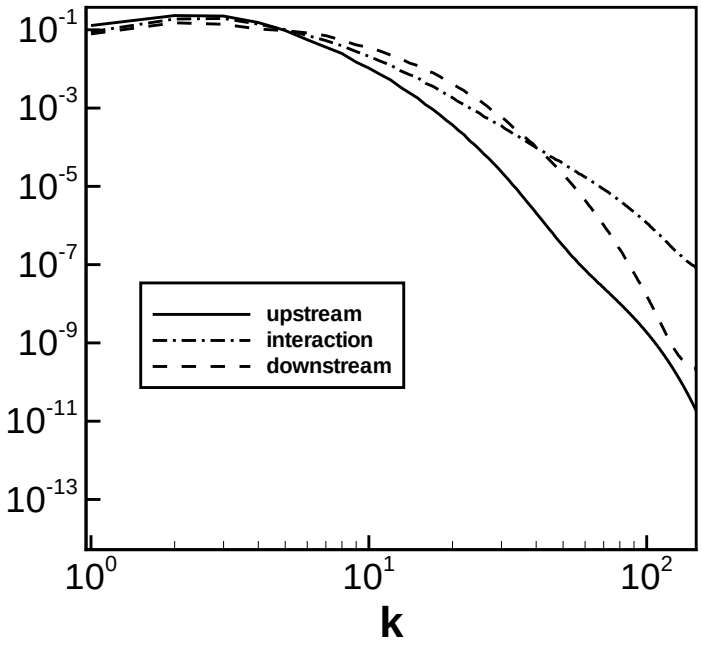

Figure 6. Two-dimensional spectra for case C1 ($M_1 = 3.46$, $M_t = 0.52$, $Re_\lambda = 26$). Spectra are plotted at planes representative of the upstream, interaction, and downstream regions. Spectra change only slightly with streamwise coordinate outside of interaction region.

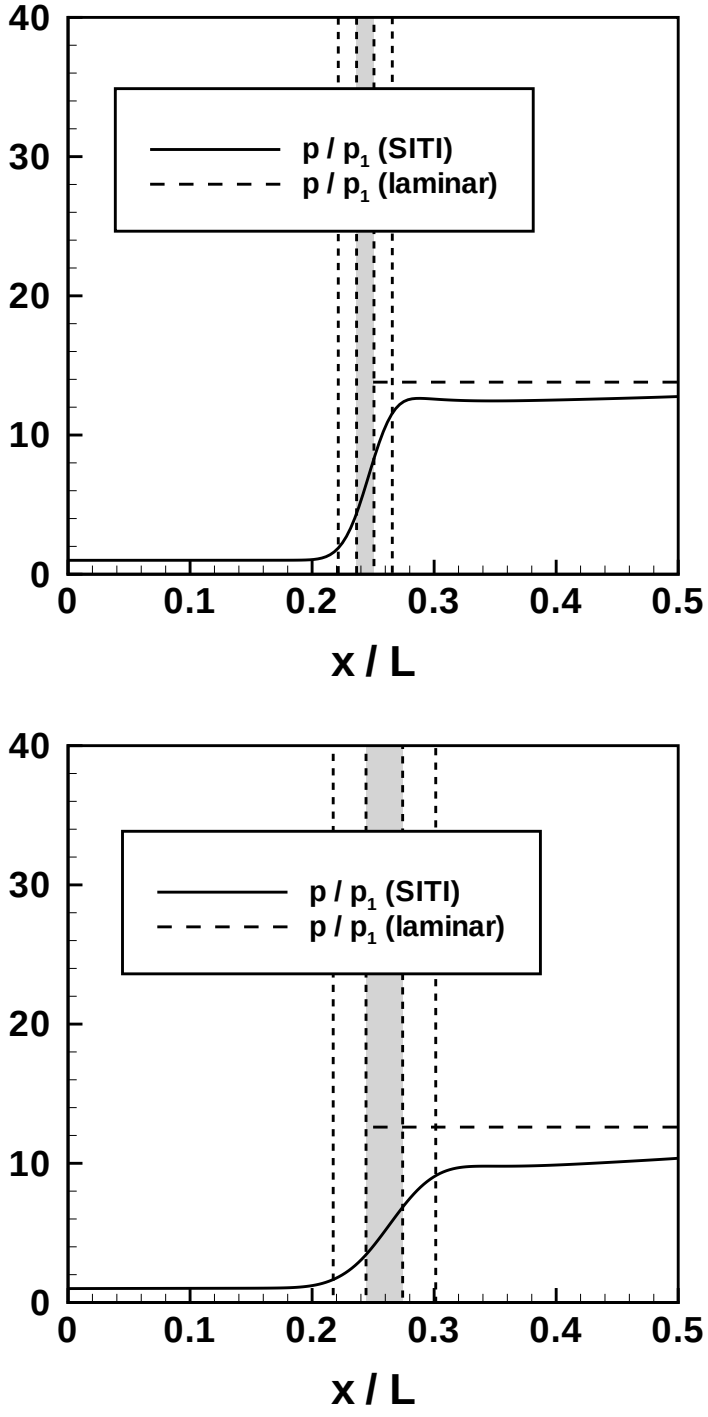

Figure 7. Density jumps across shock: *(a)* **C1** ($M_t = 0.52$) **and** *(b)* **C2** ($M_t = 0.86$)**. Laminar jump at same nominal Mach number shown for comparison.**

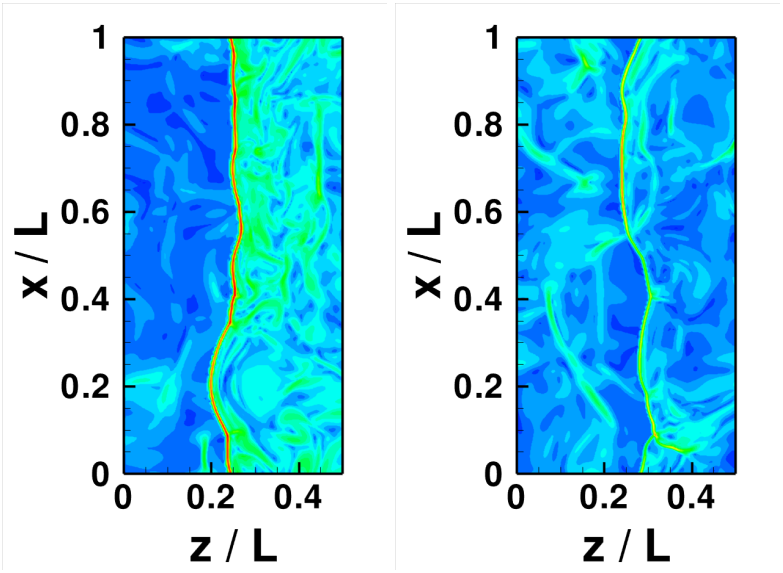

Figure 8. Instantaneous contours of density gradient magnitude $|\nabla\rho| \,/\, \langle\rho\rangle$ for cases C1 ($M_t = 0.52$), left, and C2 ($M_t = 0.86$), right. Color mappings are nonlinear and adjusted on a case-by-case basis for maximum visibility and cannot be compared between cases.

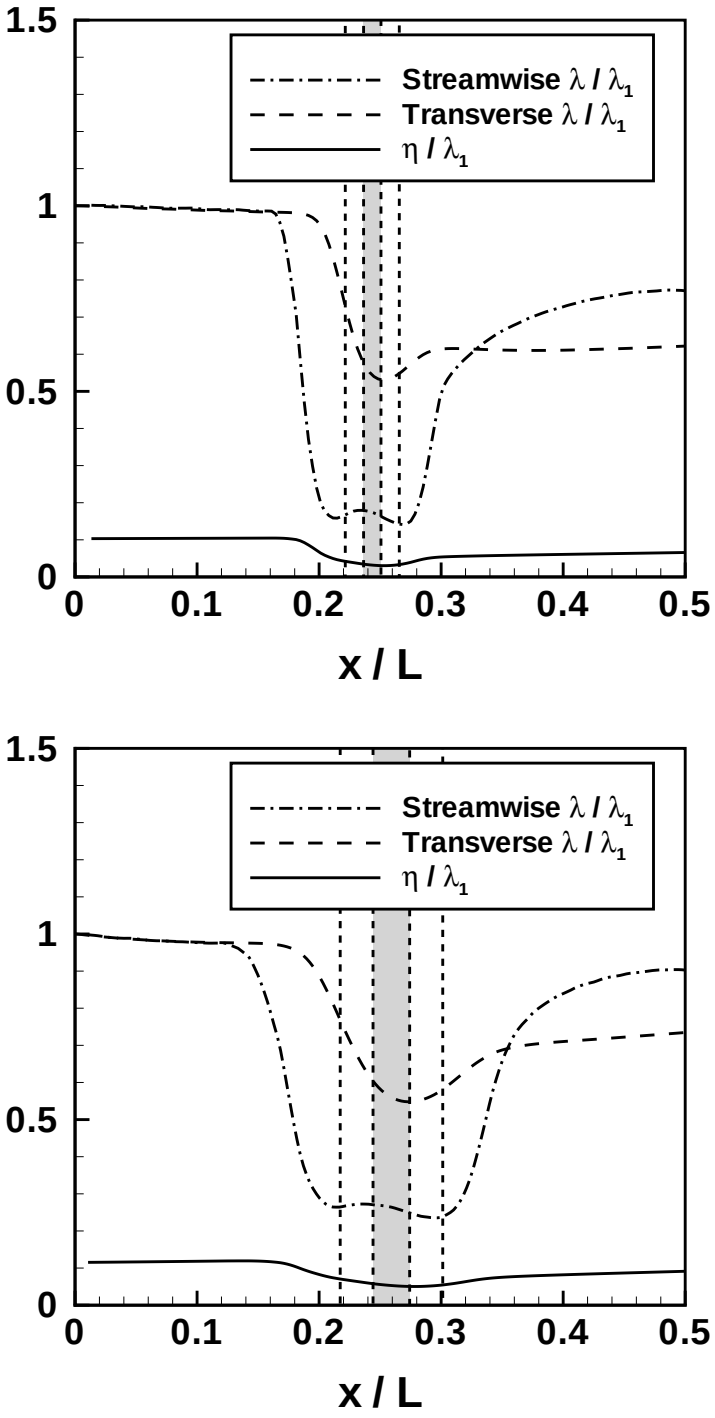

Figure 9. Profiles of Taylor microscales and Kolmogorov scale: *(a)* **C1** ($M_t = 0.52$) **and** *(b)* **C2** ($M_t = 0.86$).

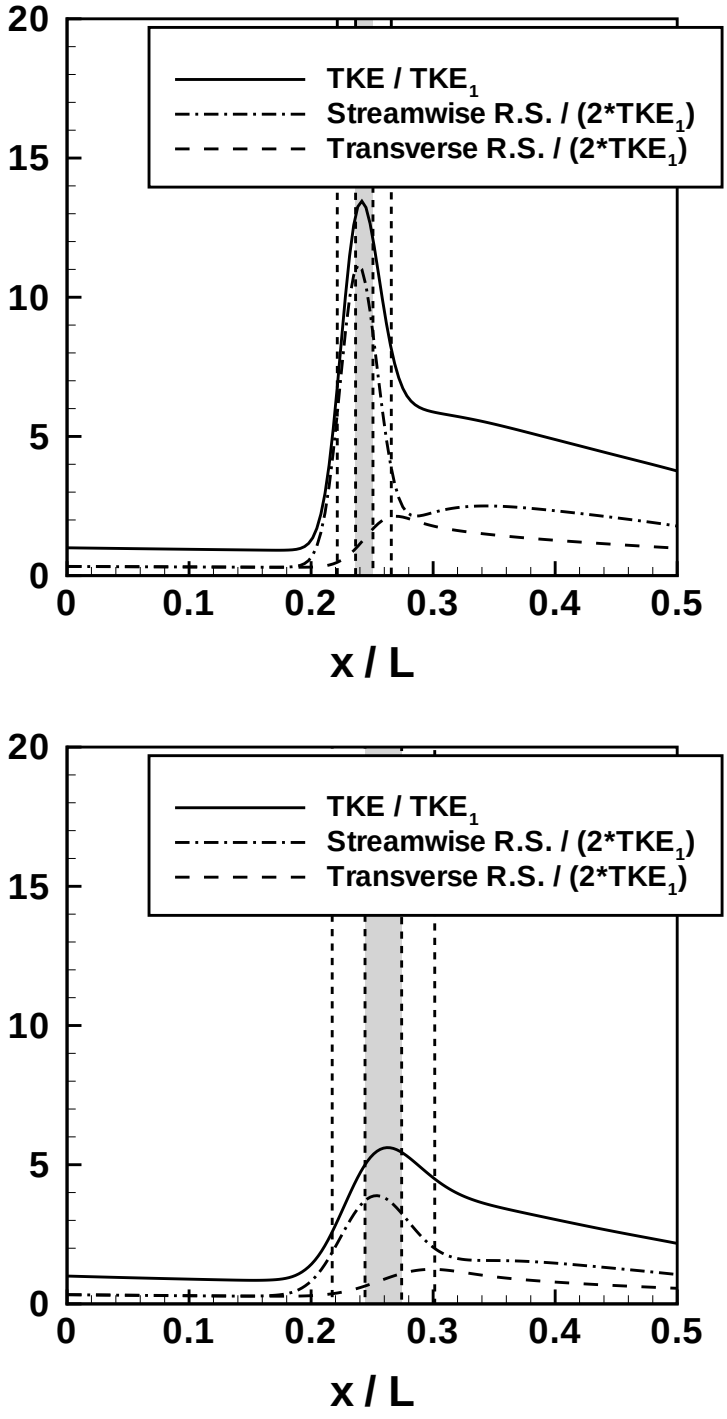

Figure 10. Turbulent kinetic energy and Reynolds stress amplification: *(a)* **C1** ($M_t = 0.52$) **and** *(b)* **C2** ($M_t = 0.86$).

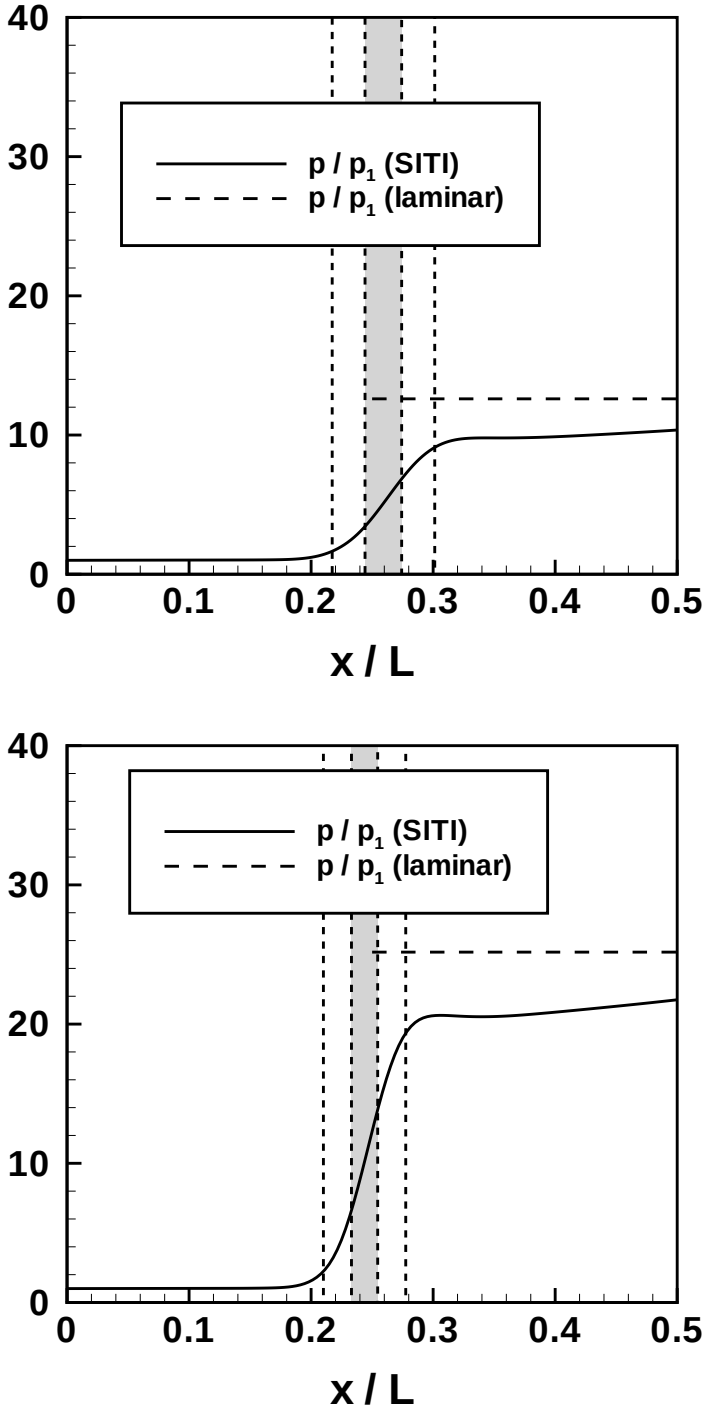

Figure 11. Density jumps across shock: *(a)* **C2** ($M = 3.31$) **and** *(b)* **C3** ($M = 4.66$)**. Laminar jump at same nominal Mach number shown for comparison.**

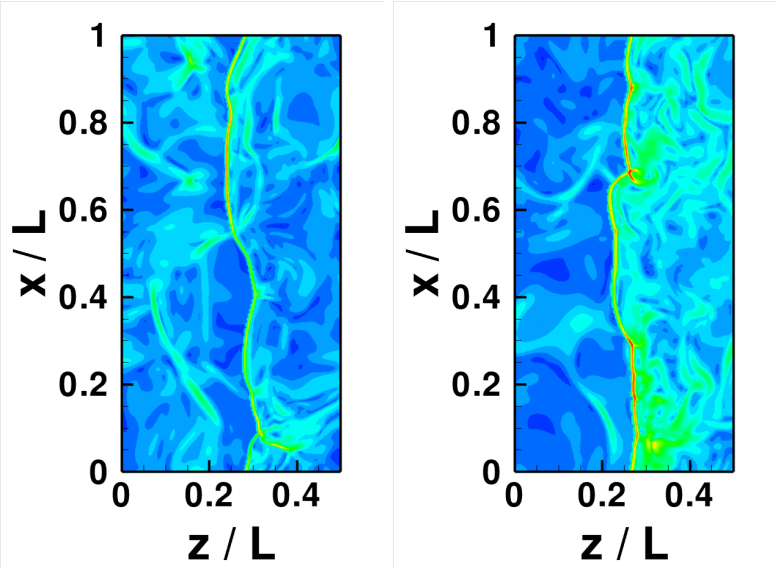

Figure 12. Instantaneous contours of density gradient magnitude $|\nabla\rho| \,/\, \langle\rho\rangle$ for cases C2 (M=3.31), left, and C3 (M=4.66), right. Color mappings are nonlinear and adjusted on a case-by-case basis for maximum visibility and cannot be compared between cases.

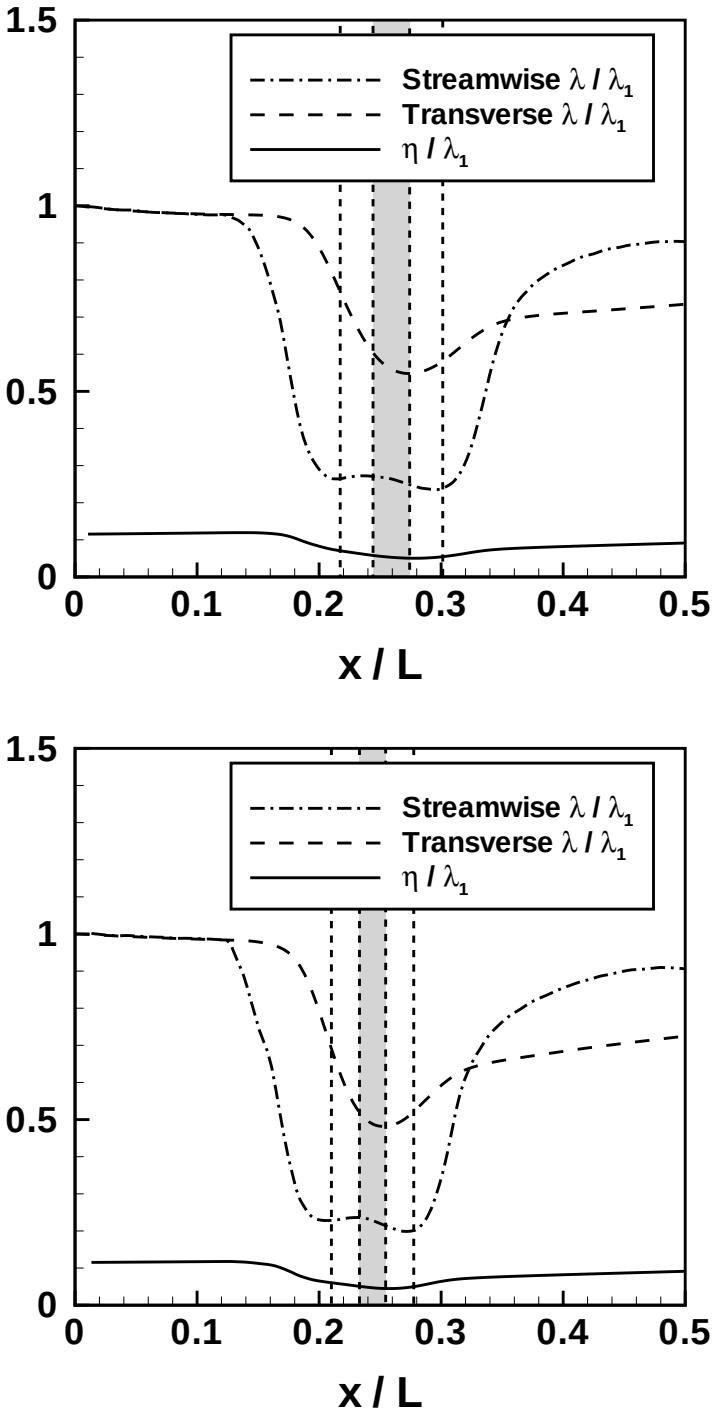

Figure 13. Profiles of Taylor microscales and Kolmogorov scale: *(a)* **C2** ($M = 3.31$) **and** *(b)* **C3** ($M = 4.66$).

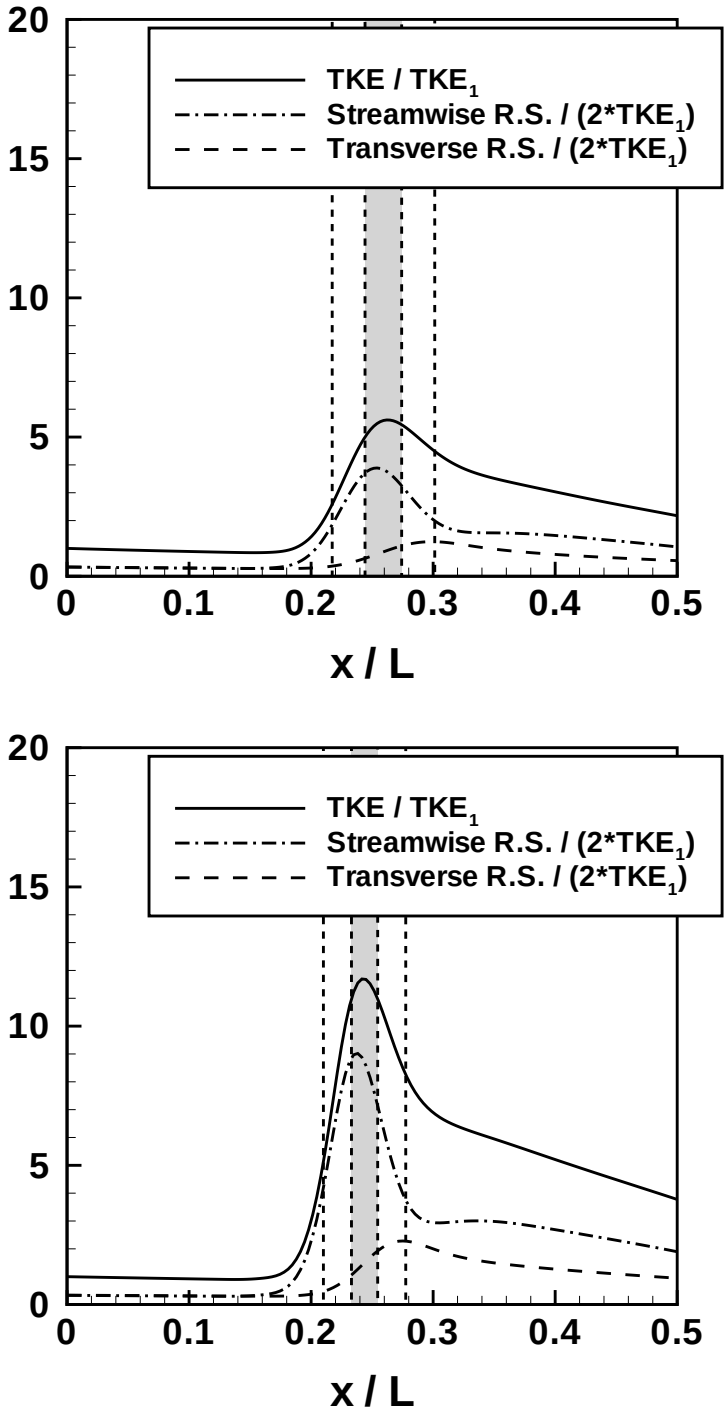

Figure 14. Turbulent kinetic energy and Reynolds stress amplification: *(a)* **C2** ($M = 3.31$) **and** *(b)* **C3** ($M = 4.66$).

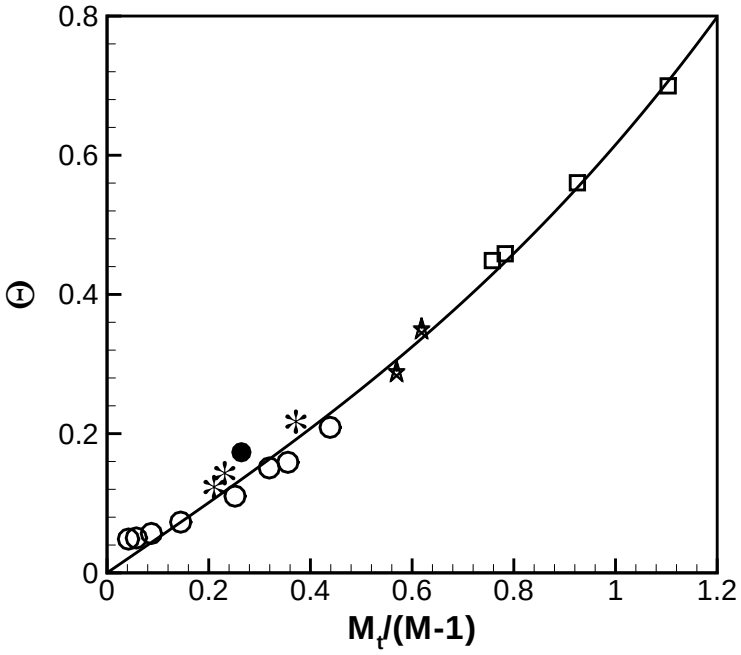

Figure 15. Normalized rms shock dilatation Θ versus $M_t/(M-1)$: data from Larsson and Lele[6](open symbols), Jamme et al.[5] (filled circle), and current results (asterisks). Data compilation and scaling from Donzis.[7]

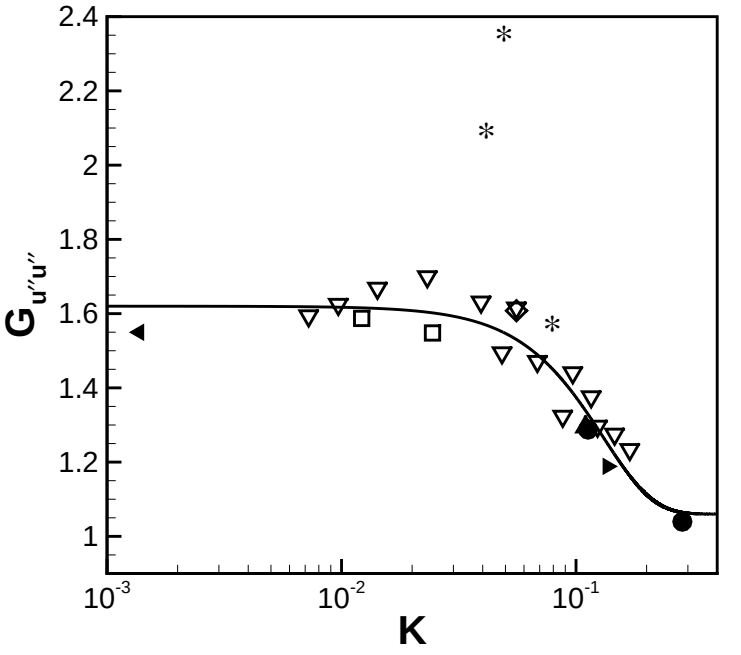

Figure 16. Streamwise velocity fluctuation variance amplification factor $G_{u''^2} \equiv u''^2_{\rm d}/u''^2_{\rm u}$ versus $K \equiv M_t/Re_\lambda^{1/2}(M-1)$: Lee et al.[24] (▶), Hannappel & Friederich[25] (◊), Barre et al.[26] (◀), Lee et al.[3] (□), Mahesh et al.[4] (▽), Jamme et al.[5] (●), Larsson & Lele[6] (△), present work (∗). Data compilation and scaling from Donzis.[7]